High performance lung nodule detection schemes in CT using local and global information

Wei Guo

School of Computer, Shenyang Aerospace University, Daoyi Development District, Shenyang, Liaoning 110136, China and Carl E. Ravin Advanced Imaging Laboratories, Department of Radiology, Duke University Medical Center, Durham, North Carolina 27705

Qiang Li[a)]

Carl E. Ravin Advanced Imaging Laboratories, Department of Radiology, Duke University Medical Center, Durham, North Carolina 27705 and Medical Imaging Information Laboratory, Shanghai Advanced Research Institute, Chinese Academy of Sciences, 99 Haike Road, Pudong District, Shanghai 201203, China

Purpose: A key issue in current computer-aided diagnostic (CAD) schemes for nodule detection in CT is the large number of false positives, because current schemes use only global three-dimensional (3D) information to detect nodules and discard useful local two-dimensional (2D) information. Thus, the authors integrated local and global information to markedly improve the performance levels of CAD schemes.

Methods: Our database was obtained from the standard CT lung nodule database created by the Lung Image Database Consortium (LIDC). It consisted of 85 CT scans with 111 nodules of 3 mm or larger in diameter. The 111 nodules were confirmed by at least two of the four radiologists participated in the LIDC. Twenty-six nodules were missed by two of the four radiologists and were thus very difficult to detect. The authors developed five CAD schemes for nodule detection in CT using global 3D information (3D scheme), local 2D information (2D scheme), and both local and global information (2D + 3D scheme, 2D − 3D scheme, and 3D − 2D scheme). The 3D scheme, which was developed previously, used only global 3D information and discarded local 2D information, as other CAD schemes did. The 2D scheme used a uniform viewpoint reformation technique to decompose a 3D nodule candidate into a set of 2D reformatted images generated from representative viewpoints, and selected and used "effective" 2D reformatted images to remove false positives. The 2D + 3D scheme, 2D − 3D scheme, and 3D − 2D scheme used complementary local and global information in different ways to further improve the performance of lung nodule detection. The authors employed a leave-one-scan-out testing method for evaluation of the performance levels of the five CAD schemes.

Results: At the sensitivities of 85%, 80%, and 75%, the existing 3D scheme reported 17.3, 7.4, and 2.8 false positives per scan, respectively; the 2D scheme improved the detection performance and reduced the numbers of false positives to 7.6, 2.5, and 1.3 per scan; the 2D + 3D scheme further reduced those to 2.7, 1.9, and 0.6 per scan; the 2D − 3D scheme reduced those to 7.6, 2.1, and 0.8 per scan; and the 3D − 2D scheme reduced those to 17.3, 1.6, and 1.0 per scan.

Conclusions: The local 2D information appears to be more useful than the global 3D information for nodule detection, particularly, when it is integrated with 3D information. © *2012 American Association of Physicists in Medicine*. [http://dx.doi.org/10.1118/1.4737109]

I. INTRODUCTION

Lung cancer is the leading cause of cancer-related mortality; American Cancer Society estimated that 157 300 lung cancer patients died in the U.S. in 2010.[1] Early detection and treatment of lung cancers is the key to improving the survival rate for patients with lung cancers. Computer-aided detection (CAD) of lung nodules in CT is one of the most active research areas in the CAD field.[2–25] Studies have shown that CAD systems for lung nodule detection have potential to detect up to half of the nodules missed by human readers and can be utilized to improve radiologists' nodule detection sensitivity.[2, 3]

In the past few years, CAD schemes for thin-section CT have been developed by many investigators. Sluimer *et al.*[4] and Li[5] reviewed the current status of CAD schemes for lung nodule detection in CT. The unique characteristics of some of the CAD schemes are briefly described below.

Bae *et al.*[6] used a morphological matching algorithm for initial identification of three categories of nodules. Messay *et al.*[7] combined intensity thresholding with morphological processing to detect and segment nodules simultaneously. Zhao *et al.*[8] employed a local density maximum algorithm to identify the nodules with high-density structures. Pu *et al.*[9] applied a simple and robust geometric model using the signed

distance field for identifying suspicious nodules. Dehmeshki *et al.*[10] developed a shape-based genetic algorithm to detect the nodules with spherical elements. McCulloch *et al.*[11] developed a model-based CAD algorithm for nodule detection, which used a Bayesian statistical model selection framework.

Enhancement algorithms were employed for nodule identification in some CAD schemes. Li *et al.*[12] developed a selective dot-enhancement filter based on Hessian matrix diagonalization for simultaneous enhancement of nodules and suppression of other normal anatomic structures such as blood vessels and airway walls, which were the main sources of false positives for nodule detection in CT. Paik *et al.*[13] developed a nodule enhancement filter for identification of initial nodule candidates based on the surface normal overlap. Matsumoto *et al.*[14] employed a novel filter called quantized convergence index filter to enhance the round lesions. Ye *et al.*[15] employed the volumetric shape index map and the dot-enhancement map to enhance objects of a specific shape with high spherical elements. Riccardi *et al.*[16] employed a 3D fast radial filtering for the preliminary detection of candidate nodules.

In some CAD schemes, many false positives were removed further by analyzing the features of nodule candidates. Ge *et al.*[17] employed 3D gradient field and ellipsoid features from the volumes of interest to reduce false positives. Roy *et al.*[18] presented a number of approaches based on the 2D radial gradient index to reduce the number of false positives. Murphy *et al.*[19] applied two successive *k*-nearest-neighbor classifiers to reduce false positives. Way *et al.*[20] used a linear discriminant analysis classifier with a stepwise feature selection to reduce false positives. Tan *et al.*[21] employed invariant features, defined on a gauge coordinates system, and a novel feature-selective classifier to reduce the false positives.

Current CAD schemes in CT produce many false positives; when the sensitivities are between 80% and 90%, the numbers of false positives are typically more than five per scan.[7–11, 13–15, 17–19] The number of false positives is large because, in large part, these CAD schemes use only global 3D information and discard useful local 2D information for lung nodule detection. In order to overcome the limitations of the 3D information, we developed a uniform viewpoint reformation technique to transform a 3D image into a series of 2D reformatted images. The primary advantage of the 3D image decomposition is that a 3D nodule appears as circular objects in nearly all the reformatted images, whereas a 3D blood vessel appears as noncircular linear objects in some "effective" reformatted images. When we take advantage of these "effective" reformatted images, we can reliably remove many blood vessels as false positives.

We developed five CAD schemes for nodule detection in CT using global 3D information (3D scheme), local 2D information (2D scheme), and both local and global information (2D + 3D scheme, 2D − 3D scheme, and 3D − 2D scheme). The performance levels for these five different schemes were evaluated and compared in this paper.

II. MATERIALS

This project was approved by Institutional Review Board at Duke University. The CT scans used in this study were obtained from the standard CT lung nodule database[22] provided by the Lung Image Database Consortium (LIDC). The database consisted of 85 CT scans, each of which contained 0–8 nodules. The tube exposure time product was 40–422 mA s, and the tube potential was 120–140 kVp. The slice thickness was 1.25–3 mm, and the interslice distance was 0.75–3 mm. Each slice had a matrix size of 512×512 pixels, and the pixel size was 0.5–0.8 mm.

The gold standard was established by a two-phase reading process. First, four radiologists who participated in the LIDC independently identified the locations and outlines of nodules of 3 mm or larger in diameter in each CT scan. After the completion of the first reading, the results were sent back to all of the four radiologists. Then, for each nodule, each radiologist either maintained his or her previous judgment or made a change by consulting the results of other three radiologists. Thirty-nine and forty-six nodules were confirmed in this two-phase reading by four and three radiologists, respectively; 26 nodules were considered as a nodule by only two of the four radiologists, and thus would be difficult to detect. In addition, 21 nodules were connected to the pleura. Figure 1 shows the histogram of the nodule sizes. It is apparent that 65% of nodules were 10 mm or smaller in diameter. Each reader delineated the contours of nodules, and we calculated the centroid of the contours. The average value of the centroids from multiple readers was used as the final centroid of the nodule.

III. METHODS

Figure 2 is the diagram of our CAD schemes for lung nodule detection using local and global information. The two steps for identification of initial nodule candidates and 3D feature determination employed the existing techniques developed by Li *et al.*[23] The other two steps in gray color in Fig. 2 were either new or extensively revised.

In the new step of the 2D feature determination, we first created multiple uniformly distributed viewpoints around a 3D nodule candidate, and reconstructed 2D reformatted images from these viewpoints. The 2D reformatted images passed the center of the nodule candidate, and were perpendicular to the radial lines connecting the center of the nodule candidate and the viewpoints. We then used an active contour model based on the region and edge to segment the nodule candidates in the 2D reformatted images, and determined the 2D features based on the shape and gradient of the nodule candidates.

In the revised step of the false-positive reduction, a stepwise classifier with minimized overtraining bias was employed to remove false positives.[23, 24] Five different classification schemes were developed based on the different sets of features for the classifier, including the 2D scheme (using 2D features only), 3D scheme (using 3D features only), 2D + 3D scheme (concurrently using 2D and 3D features), 2D − 3D
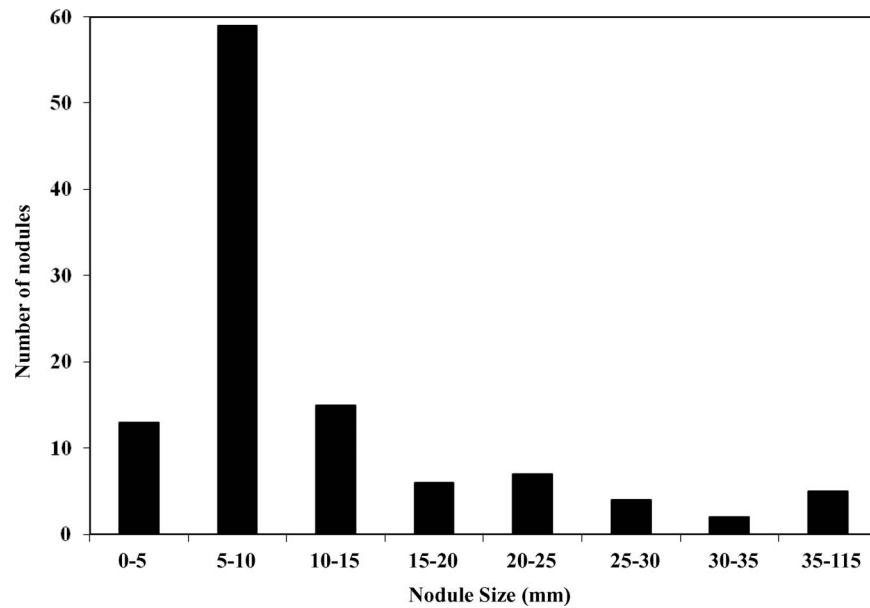
FIG. 1. Histogram of the nodule size.

scheme (using 2D features first then 3D features), and 3D − 2D scheme (using 3D features first then 2D features).

We briefly describe the existing steps for the identification of initial nodule candidates and the 3D feature determination, and focus on the steps for the 2D feature determination and the revised classification schemes.

III.A. Identification of initial nodule candidates

For identification of initial nodule candidates, the lung region of interest was first segmented from other regions using a thresholding technique,[23] and the outline of the lung region was then trimmed in order to include nodules connected to the pleura. A selective nodule enhancement filter[12] was then employed to simultaneously enhance nodules (spherical struc-

tures) and suppress normal anatomic structures, which was designed with five smoothing scales of 1, 1.6, 2.4, 3.8, and 6 mm based on the size of nodules. The line- and plane-enhancement filters were also employed to enhance blood vessels and airway walls, respectively. Finally, initial nodule candidates in the nodule-enhanced images were identified by use of a fixed, empirically selected value of 40.[23] The centers of the initial nodule candidates were used to determine the 2D and 3D features.

III.B. 3D feature determination

In the original CT images, a constrained 3D region-growing technique was employed for accurate segmentation of nodule candidates. Based on the regions of the initial and
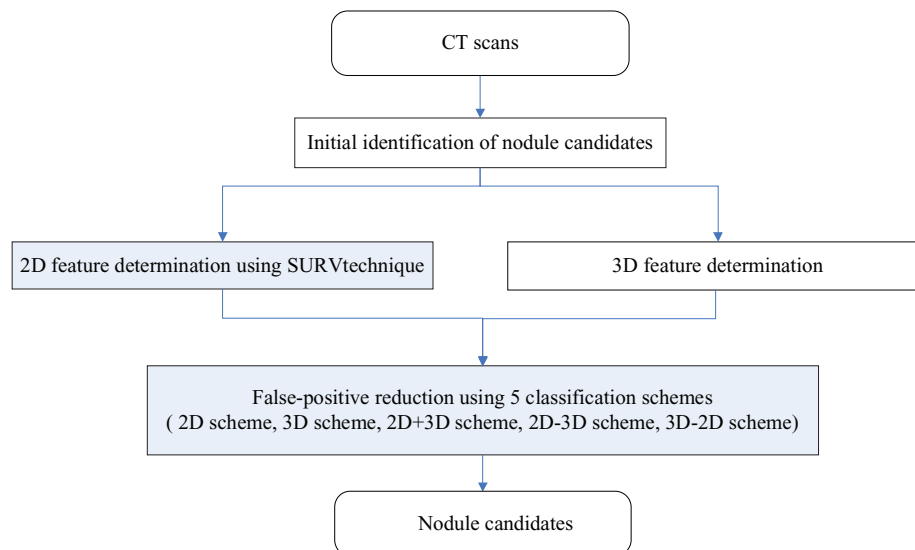

FIG. 2. Overall scheme of the computerized detection technique using 2D and 3D information.

TABLE I. Features employed in this study.

	Number of features	Name of features
2D features from a single 2D image	1	Area
	2	Effective diameter
	3	Degree of circularity
	4	Compactness
	5	Ratio of the length of the minor axis to the length of the major axis of the ellipse that had the same second moments as the region of the nodule candidate
	6	Eccentricity
	7	First moment invariant
	8	Second moment invariant
	9	Third moment invariant
	10	Maximum absolute value of the Fourier descriptors
	11	Mean of gradients of all pixels in the segmented region
2D features from multiple 2D images of a nodule candidate	12–22	Means of the features 1–11 in the other 23 2D reformatted images
	23–33	Standard deviation of the features 1–11 in the other 23 2D reformatted images
3D features	34–39	Effective diameter, degree of compactness, and irregularity determined in the initial and the grown region
	40–51	Mean and standard deviation of voxel values inside the grown region from the original, nodule-, vessel-, and airway wall-enhanced image, as well as two images of the shape index and the curvedness

grown nodule candidates, 18 features were determined based on shape and gray scale from the original, nodule-, vessel-, and airway wall-enhanced images, as well as two images of the shape index and the curvedness. These features represent the 3D global information of a 3D nodule candidate. The 3D features were listed in the lower part of Table I, and described in the paper of Li *et al.*[23]

III.C. 2D features determination

III.C.1. Reconstruction of the 2D reformatted images

A spiral scanning technique was proposed by our group[25] for 3D lung nodule segmentation. This technique can simplify the segmentation algorithm and improve the performance of segmentation by transforming a 3D volume of interest into a 2D image. The spiral scanning technique was adopted in this study to generate uniformly distributed viewpoints. The uniformly distributed viewpoints were generated from the "north pole" to the "south pole" on the surface of a sphere around a 3D nodule candidate, and were used to reconstruct the 2D reformatted images. Figure 3 shows the uniformly distributed viewpoints generated by use of the spiral scanning technique. The large dot indicates the center of a sphere, which represents the center of a nodule candidate, and the small dots represent the viewpoints distributed evenly on the surface of the sphere.

From each generated viewpoint, we reconstructed a 2D reformatted image that passed the center of a nodule candidate and was perpendicular to the radial line connecting the center of the nodule candidate and the viewpoint. Figure 4 shows a viewpoint P in a 3D coordinate system. The center of a nodule candidate was considered as the origin O, and the coordinate of the viewpoint P was represented by (r, θ, φ), where r was the distance between the origin O and P, and θ and φ were,

respectively, the angle between the Z axis and the radial line OP and the angle between the X axis and the projection of OP in XY plane.

In order to reconstruct the 2D reformatted image, we rotated the coordinate system to align the Z axis with the radial line OP. The coordinate (x, y, z) of a voxel before the rotation can be represented by the coordinate (x', y', z') of the voxel after the rotation by

$$\begin{bmatrix} x \\ y \\ z \end{bmatrix} = \begin{bmatrix} \cos\varphi\cos\theta & -\sin\varphi & \cos\varphi\sin\theta \\ \sin\varphi\cos\theta & \cos\varphi & \sin\varphi\sin\theta \\ -\sin\theta & 0 & \cos\theta \end{bmatrix} \begin{bmatrix} x'' \\ y'' \\ z'' \end{bmatrix}. \quad (1)$$

After the rotation, the plane $z' = 0$ in the new coordinate system was the 2D reformatted image, which passed the
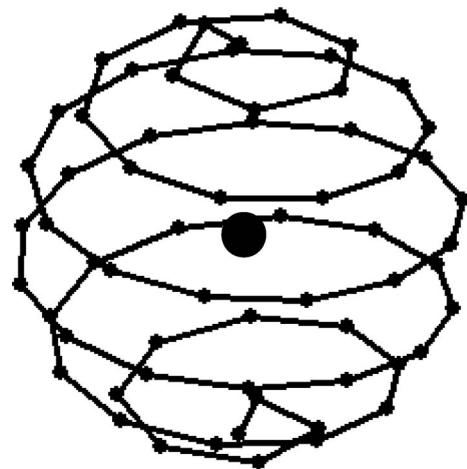

FIG. 3. Uniformly distributed viewpoints on a sphere generated by spiral-scanning technique.
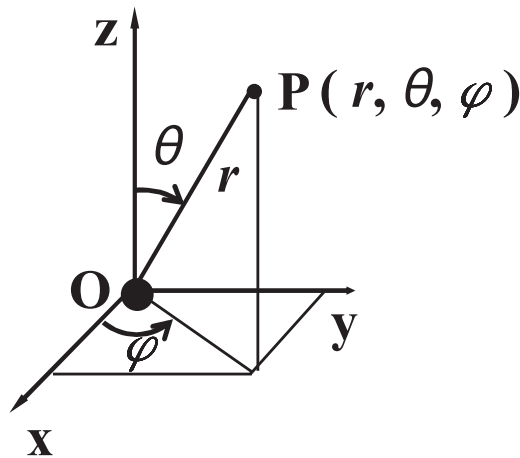
FIG. 4. Illustration of the coordinate system showing a nodule O and a viewpoint P. The reformatted 2D image generated from the viewpoint passes the center of the nodule and is perpendicular to the line connecting the center of the nodule and the viewpoint.

center of the nodule candidate and was perpendicular to the radial line OP. The gray scale of a pixel (x', y') in the 2D reformatted image was the gray scale of a voxel $(x', y', 0)$ in the 3D image after the rotation, which was employed to further determine the coordinate (x, y, z) of the corresponding voxel in the original coordinate system by use of Eq. (1). Usually the computed coordinate (x, y, z) in Eq. (1) was not located at a voxel in the original 3D image. We thus used a trilinear interpolation method to calculate the gray scale of the pixel (x', y') based on the adjacent eight voxels around the computed coordinate of (x, y, z) in the original image.

The number of the 2D reformatted images of a 3D nodule candidate was decided by the number of the viewpoints. Because the viewpoints on a sphere were roughly distributed symmetrically about the origin, the 2D reformatted images generated from the viewpoints between the "north polar" and the "equator" were similar to those between the "south polar" and the "equator." Thus, we used only the 2D reformatted images generated from the viewpoints on the upper half of the sphere in Fig. 3. We compared the performances of our CAD schemes using 11, 24, and 42 viewpoints, and found that 24 viewpoints were adequate for our CAD schemes to achieve good performance levels. Therefore, we used 24 viewpoints in this study.

Figures 5(a) and 5(b) show a 3D nodule and a 3D blood vessel (the main source of false positives) in the consecutive slices, and Figs. 5(c) and 5(d) show their 2D reformatted images. The 3D nodule in Fig. 5(a) is connected with a blood vessel, and is thus relatively difficult to be detected. However, in most of the 2D reformatted images in Fig. 5(c), the nodule appears as circular objects and is not connected with the blood vessel. Therefore, the nodule can be readily judged as a true nodule. On the other hand, the 3D blood vessel in Fig. 5(b) appears similar to a true nodule, and is likely to be detected as a nodule. However, in some 2D reformatted images in Fig. 5(d), the blood vessels appears clearly as noncircular linear objects, and can be readily classified as a blood

vessel. These useful 2D reformatted images were called the "effective" 2D reformatted images, and were used to well distinguish nodules from false positives.

III.C.2. Nodule segmentation in the 2D reformatted images

A region-based active contour model[26] was employed to segment nodule candidates in 2D reformatted images. Although the segmentation algorithm can overcome the difficulties caused by intensity inhomogeneity, it was not very accurate for the segmentation of nodule candidates with low contrast and fuzzy boundary. Therefore, an edge gradient operator was used as a constraint[27] to improve the accuracy of segmentation of nodule candidates.

The region including the center of the 2D reformatted image was considered as the segmented nodule candidate. Figures 5(e) and 5(f) show the segmentation results for the nodule and blood vessel in the 2D reformatted images. The segmented nodule in Fig. 5(e) appears as circular objects, whereas the segmented blood vessel in Fig. 5(f) appears as circular objects in some 2D reformatted images, and as noncircular linear objects in the other 2D reformatted images. Thus, the difference in the shape between nodules and false positives enabled us to distinguish between nodules and false positives.

III.C.3. 2D feature determination

Table I shows the 2D and 3D features. The 2D features were classified into two categories: the ones calculated from a single 2D reformatted image and the ones from multiple 2D reformatted images of a nodule candidate. Because a 3D nodule candidate consisted of 24 2D reformatted images, 24 sets of 2D features were determined for a 3D nodule candidate. The 2D features determined from a single 2D image included the area, effective diameter, degree of circularity, compactness, the ratio of the length of the minor axis to the length of the major axis of the ellipse that had the same second moments as the region of the nodule candidate, eccentricity, the first three moment invariants,[28,29] the maximum absolute value of the Fourier descriptors, and the mean of the gradients of all pixels in the segmented region. We found that the last four moment invariants represented very subtle details, and lacked power to represent the main characteristics of the nodule candidates. Thus, they were not able to well distinguish nodules from false positives, and were discarded. The maximum absolute value of the Fourier descriptors was used for its excellent ability in representing the shape of the nodule candidates. The definitions and meanings of these features were provided in Gonzalez et al.[29] The interval for calculating gradients was 2 pixels.

The 2D features determined from the multiple 2D images were the means and standard deviations of the 2D features in the 24 2D image of a 3D nodule. Because the shapes of the 24 2D nodules of a 3D nodule were similar to one another, the standard deviations of features were very small for nodules. On the other hand, the shapes of the 24 2D false positives of a
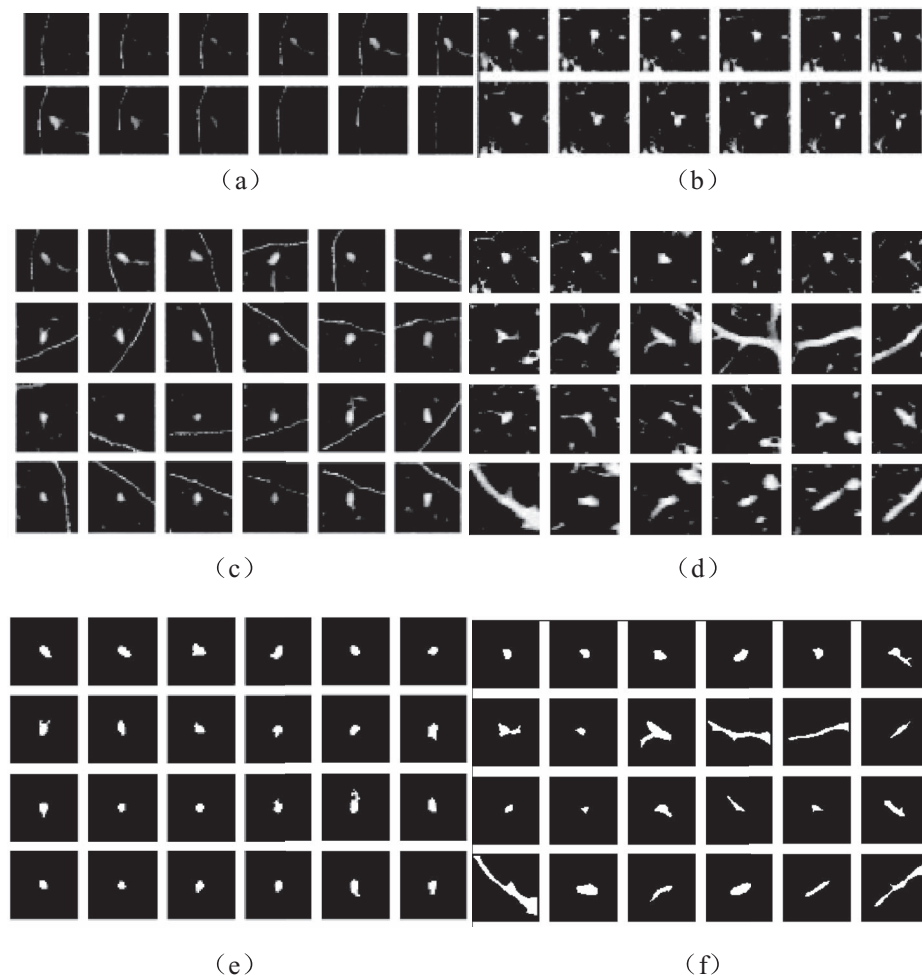
FIG. 5. A nodule (left column) and a blood vessel (right column) in the consecutive CT slices [(a) and (b)], the 2D reformatted images [(c) and (d)], and the segmented images [(e) and (f)]. As expected, the nodule appears circular in all the consecutive CT slices and 2D reformatted images. Although the blood vessel appears as nodule-like circular objects in all the consecutive CT slices, it appears clearly as noncircular linear structures in some "effective" 2D reformatted images. These "effective" 2D reformatted images enable us to well distinguish nodules from blood vessels.

3D false positive were often different from one another. Thus, the standard deviations of features were large for false positives. For each 2D reformatted image, the means and standard deviations were calculated by use of the other 23 2D reformatted images in order to make the two features slightly different across the 24 2D reformatted images. Figure 6 shows the means and standard deviations of the circularity for nodules and false positives. The means of the circularity for most of nodules are higher than those for false positives in Fig. 6, whereas the standard deviations for nodules are lower than those for false positives, which is consistent with our expectation. Therefore, we can use these two features to remove many false positives.

III.D. Feature selection and classification

Because the number of false positives was very large and many of them can be readily separated from true nodules, we employed two rules to remove many obvious false positivists. If (1) the standard deviation of the ratio of the length of the minor axis to the length of the major axis was less than 0.2, and (2) the standard deviation of the first moment invari-

ant was less than 0.5, the object was considered as a nodule and retained. Otherwise, the object was considered as a false positive and removed. The rules were determined based on the feature values of the true nodules and false positives in the entire set of 85 CT scans. Figure 7 shows the two rules
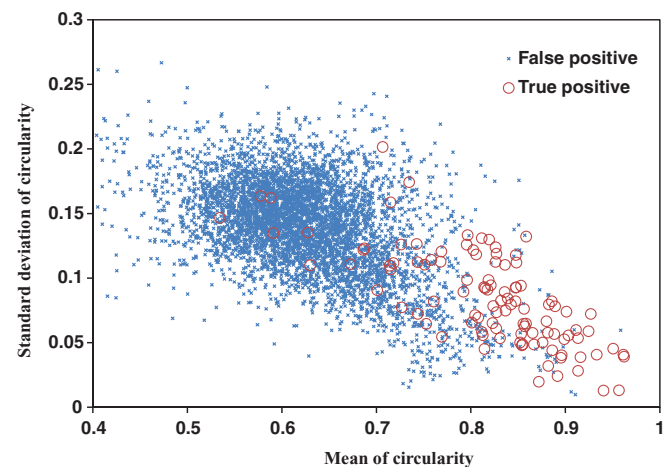

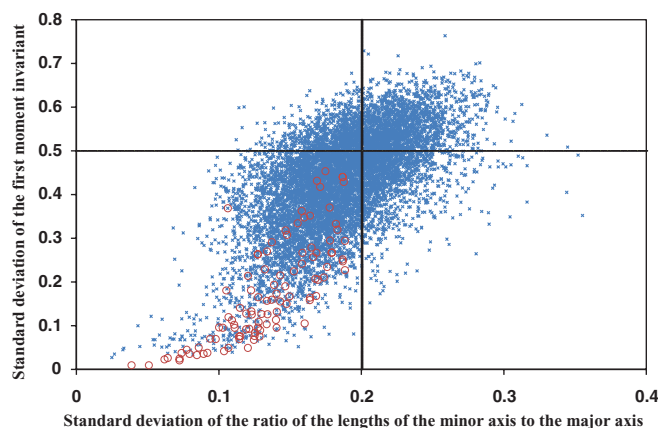FIG. 6. Relationship between two 2D features for nodules (circle) and false positives (dot).

FIG. 7. Two rules for removing many false positives. The lines, circles, and dots indicate the rules, nodules, and false positives, respectively.

indicated by two lines. It is apparent that many false positives can be removed by the two rules. Please note that the two rules were quite lax to allow many false positives to be retained as nodule candidates; this could minimize the optimistic bias caused by using the two rules. All true nodules and false positives were included in the scatter plots shown in Figs. 6 and 7.

We employed a stepwise classifier with minimized overtraining bias to reduce false positives.[23,24] We first selected an "optimal" subset of features, which was the linear combination of the features that maximized the separation between nodules and false positives.[23] The features were selected only once before the leave-one-scan-out testing method in order to reduce the calculating time. Because the number of the candidates was very large, the optimistic bias would be in an acceptable range.

We then classified the nodule candidates based on the "optimal" features by use of a linear classifier,[23] and automatically selected a cutoff threshold to remove some nodules and false positives.[24] Finally, the remaining nodule candidates were input into the linear classifier again, and the above steps were repeated until an expected sensitivity was reached.

We used five different schemes to classify the nodule candidates based on different sets of features. In the 2D scheme, we used only 2D features (features 1–33 in Table I), and treated each 2D nodule candidate independently. If at least 70% of the 2D nodule candidates of a 3D nodule candidate were classified as true nodules, the 3D nodule candidate was retained as a true nodule. Otherwise, it was discarded as a false positive. The percentage threshold of 70% was determined by analyzing the effect of the threshold on the performance of nodule detection, as described in Sec. IV.

The 3D scheme was exactly the same as that described in Li et al.[23] It used the 3D features (features 34–51 in Table I) to distinguish between nodules and false positives by use of the multiple-step linear classifier.

The 2D + 3D scheme was similar to the 2D scheme, but it used all the 2D and 3D features (features 1–51) concurrently. Please note that we assigned the 18 3D features to all the 24 2D nodule candidates of the 3D nodule candidate.

The 2D − 3D scheme employed the 2D scheme to remove some true nodules and false positives by use of the 2D features until the sensitivity reached 85%, and then used the 3D scheme to classify the remaining nodule candidates into nodules and false positives by use of the 3D features.

The 3D − 2D scheme was similar to the 2D − 3D scheme, but it employed the 3D scheme first, followed by the 2D scheme.

III.E. Evaluation methodologies

The performance levels of our CAD schemes for nodule detection were evaluated by comparing the computer-identified locations with the predetermined locations of the centers of nodules. If the distance between the center of a candidate and that of a true nodule was less than 9 mm, the nodule was considered as a detected one; otherwise, it was considered as one missed by the CAD schemes. Please note that we also visually confirmed that nodule candidates satisfying the criterion were true nodules.

A leave-one-scan-out testing method was employed for evaluating the performance levels of the five CAD schemes. The CT scan of a subject was first selected as a test image, and the CT scans of the other 84 subjects were used to train a CAD scheme. The trained CAD scheme was then applied to the test CT scan for detecting nodule candidates. This process was repeated 85 times, each for a specific subject, to complete the leave-one-scan-out evaluation method.

The performance levels of our CAD schemes were measured with a free-response receiver operating characteristic (FROC) curve.[30] The number of false positives per image at the three detection sensitivities 85%, 80%, and 75% were also reported.

IV. RESULTS

IV.A. Effect of the number of viewpoints on the performance of nodule detection

Figure 8 shows the FROC curves for the 2D + 3D scheme with 11, 24, and 42 viewpoints. The maximum number of
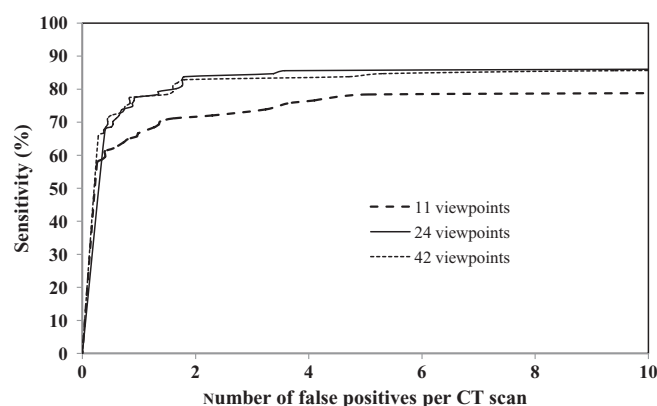

FIG. 8. FROC curves of the 2D + 3D scheme obtained with different numbers of viewpoints. The performance levels using 24 and 42 viewpoints are considerably higher than that using 11 viewpoints.
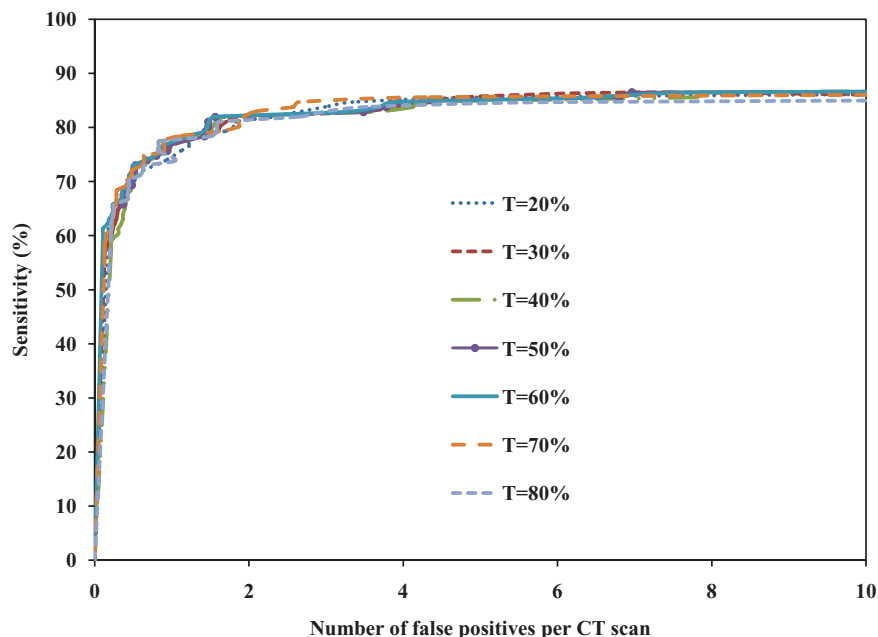
FIG. 9. FROC curves of the 2D + 3D scheme obtained with different percentage threshold (T). The performance levels using different percentage thresholds are close to one another.

false positives per scan (the horizontal axis) was set to 10 for clarity. In this experiment, we used the two rules described in Sec. III.D, and set the percentage threshold to 70%. The performance levels of 24 and 42 viewpoints were close to each other, and they were higher than that of 11 viewpoints. This was probably because the use of 11 2D reformatted images of a 3D nodule candidate did not convey adequate information for the 3D nodule candidate. The time to calculate 42 2D reformatted images was about 75% higher than that to calculate 24 2D reformatted images. We thus used 24 viewpoints in all the experiments below.

IV.B. Effect of the percentage threshold on the performance of nodule detection

Figure 9 shows the FROC curves for the 2D + 3D scheme with the different percentage thresholds of 20%, 30%, 40%, 50%, 60%, 70%, and 80%. In this experiment, the number of viewpoints was 24, and the two rules were employed. The performance levels of the 2D + 3D scheme did not change significantly for the different percentage thresholds. Thus, the 2D + 3D scheme was relatively stable (insensitive) to the change of thresholds. When the percentage thresholds ranged from 40% to 70%, the performance levels were relatively higher than the other thresholds. Therefore, we selected 70% as the percentage threshold in this study.

IV.C. Effect of the rules on the performance of nodule detection and needed time

As described in Sec. III.D, two simple rules were used to remove many false positives before the use of the piecewise linear classification. Our initial detection scheme identified 9155 3D nodule candidates with 219 720 (=9155 × 24) 2D

reformatted images. It would take a very long time to process all these images and their related features. After the first rule was applied, 80 090 2D false positives were removed and all the true nodules were retained. After the second rule was applied, additional 22 201 2D false positives were removed with all the true nodules retained.

Figure 10 shows the FROC curves for the 2D + 3D scheme with no rule, one rule, and two rules. In this study, we used 24 2D reformatted images, and set the percentage threshold to 70%. Overall, the performance levels with no rule, one rule, and two rules were very close to one another. We thus believe that the potential bias caused by use of the two rules would be minimal.

Figure 11 shows the time required to classify all 2D nodule candidates at different levels of sensitivity of the 2D + 3D scheme with no rule, one rule, and two rules. We used
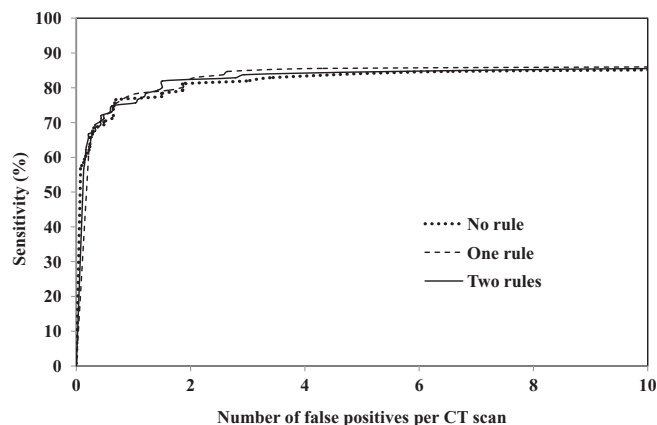

FIG. 10. FROC curves of 2D + 3D scheme obtained with no rule, one rule, and two rules. The performance levels using no rule, one rule, and two rules are close to one another.
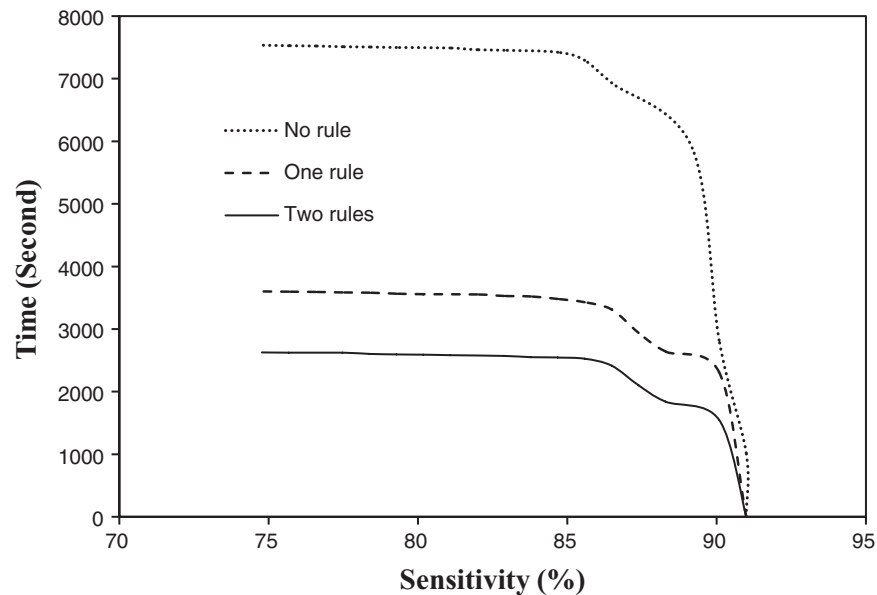
FIG. 11. Time required to classify all 2D nodule candidates at different levels of sensitivity for the 2D + 3D scheme with no rule, one rule, and two rules (initial sensitivity = 91%). When the sensitivity is set at 80%, the needed time with two rules was about a third of that with no rule.

MATLAB programming language to process all 219 720 2D nodule candidates on a PC with 2.66 GHz Intel Core 2 CPU and 3 GB RAM. The calculation time with two rules was substantially shorter than those with one rule or no rule. When the sensitivity was set at 80%, the needed times for the 2D + 3D scheme to process all 85 CT scans were 7489, 3566, and 2588 s with no rule, one rule, and two rules, respectively.

IV.D. Comparison of the performance levels with different reference standards

Figure 12 shows the FROC curves of the 2D + 3D scheme with "true" nodules identified by 2, 3, and 4 radiologists. We used the two rules, 24 2D reformatted images, and a percentage threshold of 70%. As expected, the CAD scheme achieved a higher performance for nodules identified by more radiologists.

IV.E. Comparison of the performance levels for different schemes

Figure 13 shows the FROC curves of nodule detection for the 2D scheme, 3D scheme, 2D + 3D scheme, 2D − 3D scheme, and 3D − 2D scheme. We used the two rules, 24 2D reformatted images, and a percentage threshold of 70%. Table II shows the performance levels of the five different schemes. At the sensitivities of 85% and 75%, the 2D + 3D scheme reported the best results of 2.7 and 0.6 false positives per scan (boldface in Table II), respectively. At the sensitivity of 80%, the 3D − 2D scheme reported the best result of 1.6 false positives per scan.

We employed McNemar's test to assess the statistical significance of difference in the number of false positives per scan at a fixed sensitivity of 80%. The statistical significance level was set to 0.05. The difference in false positive rate between the 3D scheme and 2D scheme was statistically significant ($p < 0.001$), which means that in our study
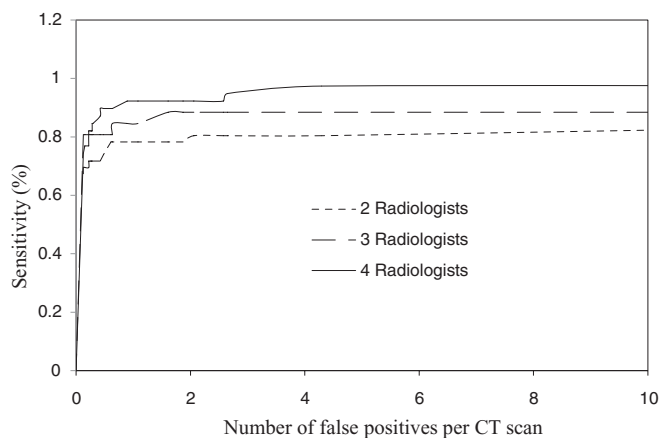

FIG. 12. FROC curves of the 2D + 3D scheme obtained with nodules confirmed by two, three, or four radiologists. If the nodules were confirmed by more radiologists, the performance of our CAD schemes for these nodules were higher.

TABLE II. The sensitivity and number of false positives of the five CAD schemes.

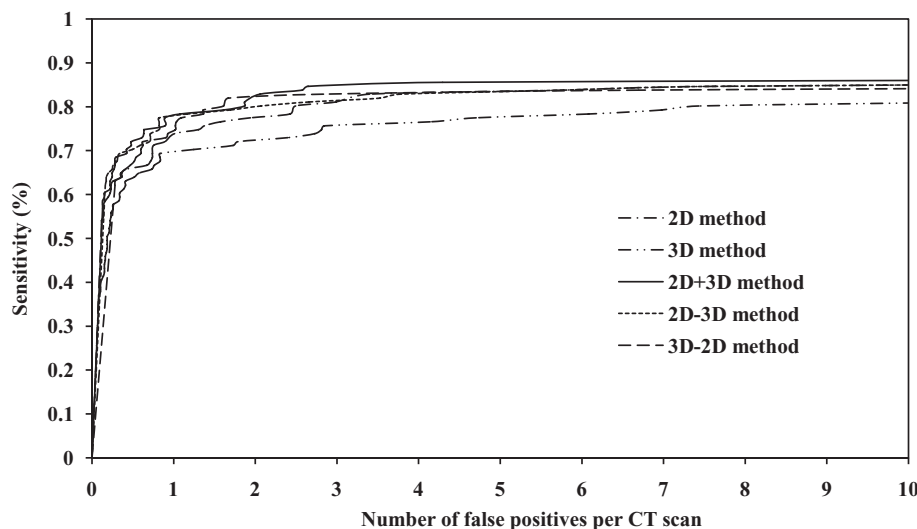|	False positive rate		
	Sensitivity = 85% (FPs/scan)	Sensitivity = 80% (FPs/scan)	Sensitivity = 75% (FPs/scan)
2D scheme	7.6	2.5	1.3
3D scheme	17.3	7.4	2.8
2D + 3D scheme	**2.7**	1.9	**0.6**
2D − 3D scheme	7.6	2.1	0.8
3D − 2D scheme	17.3	**1.6**	1.0

FIG. 13. FROC curves for the 2D scheme, 3D scheme, 2D + 3D scheme, 2D − 3D scheme, and 3D − 2D scheme. The performance levels of nodule detection using local 2D information and global 3D information (2D + 3D scheme, 2D − 3D scheme, and 3D − 2D scheme) are higher than that using 2D information alone (2D scheme). The performance of nodule detection using 3D information alone (3D scheme) is the lowest.

the 2D features seemed to be more useful than the 3D features. The difference between the 2D + 3D scheme and 3D scheme ($p < 0.001$), the 2D + 3D scheme and 2D scheme ($p < 0.001$), and the 2D + 3D scheme and 3D − 2D scheme ($p = 0.036$) were statistically significant, which means that the 2D + 3D method achieved a higher performance than the other three methods; however, the difference between the 2D + 3D scheme and 2D − 3D scheme was not statistically significant ($p = 0.15$).

V. DISCUSSION

The main issue of current CAD schemes is the large number of false positives, and that may be because they used only 3D global information. In order to overcome the limitations of the 3D information, we proposed the 2D scheme using 2D local information. The concept of this scheme has not been explored for lung nodule detection.

Although the concept of this scheme has been explored for polyps in CT colonography,[31] the implementation of our scheme is simpler and more elegant. The method for polyp detection in Ref. 31 utilized randomly selected viewpoints to generate 2D images for covering the entire lesion, whereas we systematically generated 2D reformatted images from the uniformly distributed viewpoints around a 3D nodule candidate. It appears that our method is more efficient and effective in selecting the viewpoints to cover the entire lesion. Furthermore, at each viewpoint, three orthogonal planes were utilized in Ref. 31 for generating the 2D images, whereas only one plane was utilized in our method for generating the 2D image. We believe that one 2D image is adequate for a single viewpoint, because we can readily generate denser viewpoints to better cover the lesion if needed. Therefore, our method appears again more efficient in this respect.

The primary advantage of the local 2D information is its ability to clearly represent the difference in appearance between a real nodule and a non-nodule. Whereas a 3D nodule will appear as circular objects in the reformatted 2D images from nearly all viewpoints, a 3D blood vessel appears as noncircular linear objects in some "effective" reformatted images, and as nodule-like circular objects in the other "ineffective" reformatted images. When we take advantage of these "effective" reformatted images, we can reliably remove many blood vessels. Using the global 3D information alone is similar to mixing the local 2D information from some "effective" reformatted images and that from many "ineffective" reformatted images, and thus obscures the significance of the local 2D information from the "effective" reformatted images. This concept is also useful for removing the false positives of other types, such as those caused by soft tissue around mediastinum or diaphragm.

Another advantage of the local 2D information is the usefulness of the variation in the shape of a nodule candidate across all 2D reformatted images. The variation in the shape of a blood vessel across all reformatted images is generally large, whereas that of a nodule is small. Thus, we employed the variation in the shape of a nodule candidate to remove many false positives.

The third advantage of the 2D scheme was the considerable increase in the number of true nodules created by transforming a single 3D nodule into 24 (though correlated) 2D nodules in the reformatted 2D images. The increase in the number of training true nodules might be able to improve the robustness and generalizability of our CAD schemes for nodule detection in unseen future CT scans.

Although the performance of nodule detection using the local 2D information was higher than that using the global 3D information, it was the combination of the local and global information that further improved the performance of nodule detection. In this study, three schemes were developed to combine the 2D and 3D information, including the 2D + 3D scheme, the 2D − 3D scheme, and the 3D − 2D scheme. The

performance levels of these three schemes were close to one another, and the performance of the 2D + 3D scheme was slightly higher than those of the other two schemes. Our CAD schemes using both 2D and 3D information challenged the architecture of current CAD schemes developed in 3D imaging modalities, and would have broad scientific impact on detection and diagnosis of many types of lesions in 3D imaging modalities.

Two rules were employed before the application of the piecewise linear classifier to reduce the calculation time, which would inevitably cause bias in the estimated performance. In order to minimize the bias, we employed only two rules and made each rule quite lax so that only the most obvious false positives were eliminated by use of the rules. As described in Sec. IV.C, the use of the two rules did not significantly affect the performance of nodule detection, and the bias caused by the two rules was limited and negligible.

We used only the nodules in the LIDC database determined by at least two of the four radiologists. If we used a set of nodules determined by a different number of radiologists, the results of nodule detection may be slightly different from those presented in this study. However, we strongly believe that the use of a different set of nodules in the LIDC database would not change the conclusion of this study; that is, the combination of the 2D and 3D information of the nodule candidates can be utilized to significantly improve the performance of nodule detection.

VI. CONCLUSION

We developed five CAD schemes for lung nodule detection using global 3D information, local 2D information, and both global and local information. Key contributions of our schemes were to decompose a 3D nodule candidate into a set of 2D reformatted images generated from many representative viewpoints, and to use the local 2D information from the 2D reformatted images for remarkably improving the performance of nodule detection. Furthermore, the integration of the complementary local and global information enabled us to achieve the highest performance for nodule detection in CT.

ACKNOWLEDGMENTS

[a]Author to whom correspondence should be addressed. Electronic mail: liqiang@sari.ac.cn

[1]A. Jemal, R. Siegel, J. Xu, and E. Ward, "Cancer statistics, 2010," CA Cancer J. Clin. **60**(5), 277–300 (2010).

[2]J. E. Roos, D. Paik, D. Olsen, L. C. Chow, A. N. Leung, R. Mindelzun, K. R. Choudhury, D. P. Naidich, S. Napel, and G. D. Rubin, "Computer-aided detection (CAD) of lung nodules in CT scans: Radiologist performance and reading time with incremental CAD assistance," Eur. Radiol. **20**(3), 549–557 (2010).

[3]F. Beyer, L. Zierott, E. M. Fallenberg, K. U. Juergens, J. Stoeckel, W. Heindel, and D. Wormanns, "Comparison of sensitivity and reading time for the use of computer-aided detection (CAD) of pulmonary nodules at MDCT as concurrent or second reader," Eur. Radiol. **17**(11), 2941–2947 (2007).

[4]I. Sluimer, A. Schilham, M. Prokop, and B. van Ginneken, "Computer analysis of computed tomography scans of the lung: A survey," IEEE Trans. Med. Imaging **25**(4), 385–405 (2006).

[5]Q. Li, "Recent progress in computer-aided diagnosis of lung nodules on thin-section CT," Comput. Med. Imaging Graph. **31**(4–5), 248–257 (2007).

[6]K. T. Bae, J. S. Kim, Y. H. Na, K. G. Kim, and J. H. Kim, "Pulmonary nodules: Automated detection on CT images with morphologic matching algorithm-preliminary results," Radiology **236**, 286–293 (2005).

[7]T. Messay, R. C. Hardie, and S. K. Rogers, "A new computationally efficient CAD system for pulmonary nodule detection in CT imagery," Med. Image Anal. **14**(3), 390–406 (2010).

[8]B. Zhao, G. Gamsu, M. S. Ginsberg, L. Jiang, and L. H. Schwartz, "Automatic detection of small lung nodules on CT utilizing a local density maximum algorithm," J. Appl. Clin. Med. Phys. **4**(3), 248–260 (2003).

[9]J. Pu, B. Zheng, J. K. Leader, X. Wang, and D. Gur, "An automated CT based lung nodule detection scheme using geometric analysis of signed distance field," Med. Phys. **35**(8), 3453–3461 (2008).

[10]J. Dehmeshki, X. Ye, X. Lin, M. Voldivieso, and H. Amin, "Automated detection of lung nodules in CT images using shape-based genetic algorithm," Comput. Med. Imaging Graph. **31**(6), 408–417 (2007).

[11]C. C. McCulloch, R. A. Kaucic, P. R. S. Mendonca, D. J. Walter, and R. S. Avila, "Model-based detection of lung nodules in computed tomography exams. Thoracic computer-aided diagnosis," Acad. Radiol. **11**(3), 258–266 (2004).

[12]Q. Li, S. Sone, and K. Doi, "Selective enhancement filters for nodules, vessels, and airway walls in two- and three-dimensional CT scans," Med. Phys. **30**(8), 2040–2051 (2003).

[13]D. S. Paik, C. F. Beaulieu, G. D. Rubin, B. Acar, R. B. Jeffrey, J. Yee, J. Dey, and S. Napel, "Surface normal overlap: A computer-aided detection algorithm with application to colonic polyps and lung nodules in helical CT," IEEE Trans. Med. Imaging **23**(6), 661–675 (2004).

[14]S. Matsumoto, H. L. Kundel, J. C. Gee, W. B. Gefter, and H. Hatabu, "Pulmonary nodule detection in CT images with quantized convergence index filter," Med. Image Anal. **10**(3), 343–352 (2006).

[15]X. Ye, X. Lin, J. Dehmeshki, G. Slabaugh, and G. Beddoe, "Shape based computer-aided detection of lung nodules in thoracic CT images," IEEE Trans. Biomed. Eng. **56**(7), 1810–1820 (2009).

[16]A. Riccardi, T. S. Petkov, G. Ferri, M. Masotti, and R. Campanini, "Computer-aided detection of lung nodules via 3D fast radial transform, scale space representation, and Zernike MIP classification," Med. Phys. **38**(4), 1962–1971 (2011).

[17]Z. Ge, B. Sahiner, H. P. Chan, P. N. Cascade, N. Bogot, E. A. Kazerooni, J. Wei, and C. Zhou, "Computer-aided detection of lung nodules: False positive reduction using a 3D gradient field method and 3D ellipsoid fitting," Med. Phys. **32**(8), 2443–2454 (2005).

[18]A. S. Roy, S. G. Armato 3rd, A. Wilson, and K. Drukker, "Automated detection of lung nodules in CT scans: False-positive reduction with the radial-gradient index," Med. Phys. **33**(4), 1133–1140 (2006).

[19]K. Murphy, B. van Ginneken, A. M. R. Schilham, B. J. de Hoop, H. A. Gietema, and M. Prokop, "A large-scale evaluation of automatic pulmonary nodule detection in chest CT using local image features and k-nearest-neighbour classification," Med. Image Anal. **13**(5), 757–770 (2009).

[20]T. W. Way, L. M. Hadjiiski, B. Sahiner, H. P. Chan, P. N. Cascde, E. A. Kazerooni, N. Bogot, and C. Zhou, "Computer-aided diagnosis of pulmonary nodules on CT scans: Segmentation and classification using 3D active contours," Med. Phys. **33**(7), 2323–2337 (2006).

[21]M. Tan, R. Deklerck, B. Jansen, M. Bister, and J. Cornelis, "A novel computer-aided lung nodule detection system for CT images," Med. Phys. **38**(10), 5630–5645 (2011).

[22]M. F. McNitt-Gray, S. G. Armato 3rd, C. R. Meyer, A. P. Reeves, G. McLennan, R. C. Pais, J. Freymann, M. S. Brown, R. M. Engelmann, P. H. Bland, G. E. Laderach, C. Piker, J. Guo, Z. Towfic, D. P. Qiang, D. F. Yankelevitz, D. R. Abrele, E. J. Van Beek, H. MacMahon, E. A. Kazerooni, B. Y. Croft, and L. P. Clarke, "The Lung Image Database Consortium

(LIDC) data collection process for nodule detection and annotation," Acad. Radiol. **14**(12), 1464–1474 (2007).

[23] Q. Li, F. Li, and K. Doi, "Computerized detection of lung nodules in thin-section CT images by use of selective enhancement filters and an automated rule-based classifier," Acad. Radiol. **15**(2), 165–175 (2008).

[24] Q. Li and K. Doi, "Analysis and minimization of overtraining effect in rule-based classifiers for computer-aided diagnosis," Med. Phys. **33**(2), 320–328 (2006).

[25] J. Wang, R. Engelmann, and Q. Li, "Segmentation of pulmonary nodules in three-dimensional CT images by use of a spiral-scanning technique," Med. Phys. **34**(12), 4678–4689 (2007).

[26] C. Li, C. Kao, J. C. Gore, and Z. Ding, "Minimization of region-scalable fitting energy for image segmentation," IEEE Trans. Image Proc. **17**(10), 1940–1949 (2008).

[27] V. Caselles, R. Kimmel, and G. Sapiro, "Geodesic active contours," Int. J. Comput. Vis. **22**(1), 61–79 (1997).

[28] M. Hu, "Visual pattern recognition by moment invariants," IRE Trans. Inform. Theory **8**(2), 179–187 (1962).

[29] R. C. Gonzalez, R. E. Woods, and E. S. L. Eddins, *Digital Image Processing Using MATLAB* (Prentice Hall, New Jersey, 2003).

[30] C. E. Metz, "Some practical issues of experimental design and data analysis in radiological ROC studies," Invest. Radiol. **24**(3), 234–245 (1989).

[31] S. B. Gokturk, C. Tomasi, B. Acar, C. F. Beaulieu, D. S. Paik, R. B. Jeffrey, Jr., J. Yee, and S. Napel, "A statistical 3-D pattern processing method for computer-aided detection of polyps in CT colonography," IEEE Trans. Med. Imaging **21**(12), 1251–60 (2001).